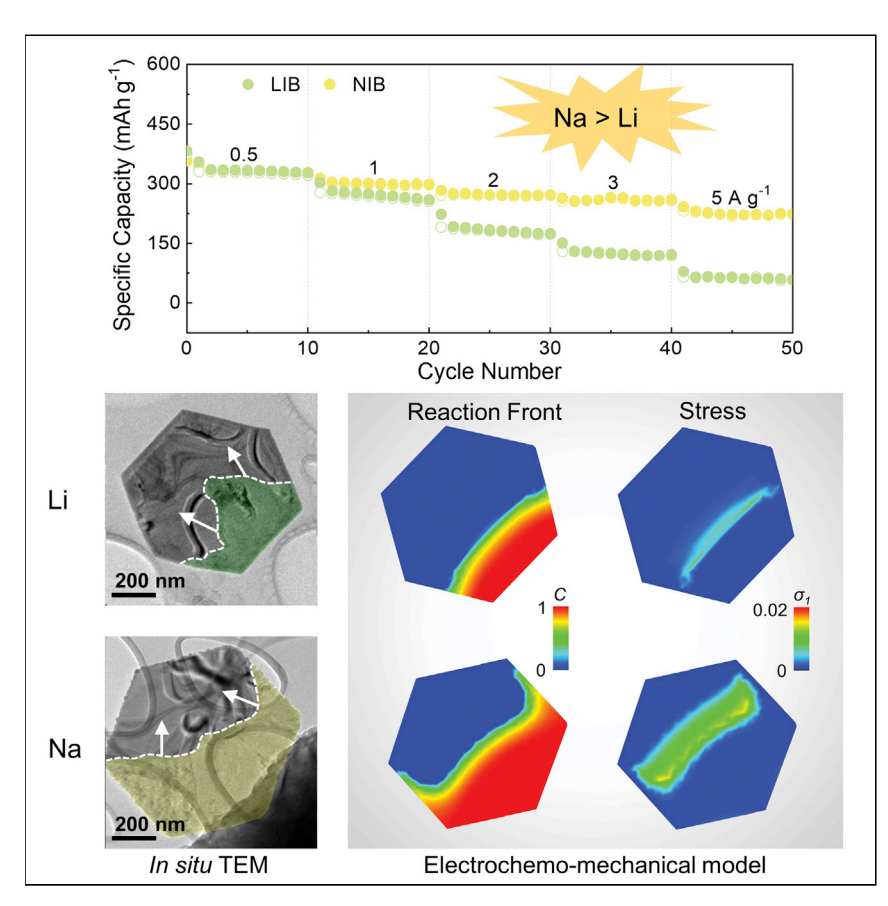
# **Matter**



## **Article**

# Origin of anomalous high-rate Na-ion electrochemistry in layered bismuth telluride anodes



Na-ion batteries were intuitively considered unfavorable for high power density due to the kinetics limitation. A comparative study of lithiation, sodiation, and potassiation of layered metal chalcogenide  ${\rm Bi_2Te_3}$  is presented to challenge this prejudice, showing unexpected high Na-ion electrochemical performance at high current densities. The systematic *in situ* transmission electron microscopy and theoretical calculation unanimously attribute the anomalous high-rate Na-ion electrochemistry to the unique phase transformation and the correlated electrochemo-mechanical stress concentration during sodiation of  ${\rm Bi_2Te_3}$ .

kaihe@clemson.edu

HIGHLIGHTS

Ultrafast Na-ion electrochemistry
outperforming Li-ion and K-ion
counterparts

Jiang Cui, Hongkui Zheng,

Xiao-Qing Yang, Kai He

Zilong Zhang, Sooyeon Hwang,

In situ TEM of comparative lithiation, sodiation, and potassiation in layered Bi<sub>2</sub>Te<sub>3</sub>

Better sodiation kinetics induced by lower interfacial strain accommodation energy

Distinct reaction propagation dominated by chemo-mechanical stress concentration



Cui et al., Matter 4, 1335–1351 April 7, 2021 © 2021 The Author(s). Published by Elsevier Inc.





# **Matter**



#### **Article**

# Origin of anomalous high-rate Na-ion electrochemistry in layered bismuth telluride anodes

Jiang Cui, Hongkui Zheng, Zilong Zhang, Sooyeon Hwang, Xiao-Qing Yang, and Kai He<sup>1,4,\*</sup>

#### **SUMMARY**

van der Waals layered metal chalcogenide Bi<sub>2</sub>Te<sub>3</sub> has shown exceptional capacity and rate capability in alkali-ion batteries but the underlying reaction mechanism with Li<sup>+</sup>, Na<sup>+</sup>, and K<sup>+</sup> remains undiscovered. It is unexpected that Na<sup>+</sup> electrochemistry outperforms Li<sup>+</sup> and K<sup>+</sup> at high current densities. Here, in situ transmission electron microscopy is used to uncover nanoscale transformations during lithiation, sodiation, and potassiation, which follows two-step conversion and alloying reactions with Li<sup>+</sup> and Na<sup>+</sup>, and three-step intercalation-conversion-alloying reactions with K<sup>+</sup>. Counterintuitively, sodiation exhibits the highest reaction kinetics, and its origin can be elucidated by first-principles and finite-element simulations in two aspects. The lower interfacial strain accommodation energy between Bi<sub>2</sub>Te<sub>3</sub> and its Na-conversion products allows more facile sodiation phase transformation than Li- and K-ion reactions. The higher electrochemo-mechanical stress concentration at the concave-shaped sodiation reaction front facilitates continued Naion diffusion and reaction propagation. These fundamental insights are essential for fast-charging alkali-ion batteries.

#### **INTRODUCTION**

Lithium-ion batteries (LIBs) have become the cornerstone of energy sustainability. LIBs are an essential component of energy storage technology for applications in portable electronics, electric vehicles, drones, and utility-scale storage systems for wind and solar plants. Such large-scale production of LIBs is rapidly depleting the precursors used for making electrode materials and driving the cost up. In recent years, there has been renewed interest in the research and development of Naion batteries (NIBs) and K-ion batteries (KIBs) as cost-effective alternatives to LIBs due to the earth abundance and the low cost of Na- and K-containing precursors.<sup>2-7</sup> Although NIBs and KIBs share similar working principles with the widely studied LIBs, it has come to light that the technically viable anode materials for NIBs and KIBs are largely distinct from those for LIBs. 8-10 For example, the commercially dominant graphite anode for LIBs exhibits negligible capacity in NIBs and KIBs. 11,12 The lack of promising anode materials has been the major obstacle hindering the development and commercialization of NIB and KIB technologies. Previous research has revealed that materials undergoing conversion reactions with Na<sup>+</sup> and  $K^{+}$  ions, such as  $FeS_{2}$ ,  $^{13}$   $MoS_{2}$ ,  $^{14}$   $Sb_{2}S_{3}$ ,  $^{15-18}$   $SnS_{2}$ ,  $^{19,20}$  and  $SnSe_{2}$ ,  $^{21}$  are among the promising anodes because of their high capacities and low electrochemical potentials.<sup>22</sup> Furthermore, many of this type of anode materials possess two-dimensional (2D) van der Waals layered crystal structures to enable fast-charging capabilities.  $^{14,17,23,24}$  For example, the anode made of  $SnS_2$  nanoplates was reported to

#### **Progress and potential**

Sodium ranks the sixth most abundant element, making it promising for cost-effective Naion batteries to complement the dominant Li-ion technology. It is generally believed that Na-ion batteries can only deliver limited power due to the sluggish electrochemical reaction kinetics. Here, through a systematic comparison of Li<sup>+</sup>, Na<sup>+</sup>, and K<sup>+</sup> reactions with van der Waals layered Bi<sub>2</sub>Te<sub>3</sub>, we reveal anomalous high-rate performance showing that sodium unexpectedly outperforms the lithium and potassium counterparts. A combination of electrochemical analysis, in situ transmission electron microscopy, first-principles calculation, and finite-element modeling is employed to elucidate the origin of this intriguing phenomenon, which provides insights into fundamental understanding of reaction mechanisms of lithiation, sodiation, and potassiation, and elucidates the reason for the superior Na storage capability. These findings open up new opportunities in making Na-ion batteries with not only low cost but also high-power performance.







functionally operate at a high current density of 10 A  $\mathrm{g}^{-1}$  in NIBs without much sacrifice of capacity, which even outperforms most LIBs, making the development of fast-charging NIBs possible.<sup>20</sup> In fact, such an anomalously facile Na storage in layered metal chalcogenide anodes has been observed in previous studies, 17,20,25,26 which is in stark contrast to other electrode materials that usually exhibit significantly inferior Na storage capability at high current densities compared with their LIB counterparts. Despite these appealing findings, the underlying mechanism of unexpected high-rate performances of metal chalcogenides remains elusive due to three major issues: (1) there still lacks a comprehensive understanding of the intricate phase transformation mechanism for van der Waals layered anodes due to difficulties in precise tracking of phase transition and separation processes; (2) the similarities and differences of phase transformations upon electrochemical reactions with different alkali ions (Li<sup>+</sup>, Na<sup>+</sup>, and K<sup>+</sup>) are largely unknown, hindering the comprehension of Na and K storage mechanisms based on the existing knowledge of LIBs; (3) it is challenging to correlate the electrochemical phase transformation with the mechanical evolution in anodes, which is crucial for the electrochemical performance of batteries.<sup>27</sup>

In situ characterization methods, <sup>28–31</sup> especially in situ transmission electron microscopy (TEM) based on nanometric electrochemical cells, have been demonstrated to quantitatively probe reaction kinetics in various electrochemical processes with atomic resolution that was previously thought infeasible by other means. 32-35 Among various metal chalcogenide candidates, Bi<sub>2</sub>Te<sub>3</sub> stands out as the material of interest in this study for three major reasons: (1) despite limited reports in battery applications, Bi<sub>2</sub>Te<sub>3</sub> turns out to possess one of the highest theoretical volumetric capacity of 3,093 mAh  $L^{-1}$ , making it a promising anode that may outperform other 2D materials; (2) the facile synthesis of single-crystalline Bi<sub>2</sub>Te<sub>3</sub> with well-defined planar hexagon morphology makes it a suitable model for quantitative in situ TEM studies; (3) Bi<sub>2</sub>Te<sub>3</sub> is expected to be electrochemically active with respect to not only Li-ion but also Na- and K-ions, which is crucial for revealing its alkali-ion storage mechanisms and electrochemo-mechanical properties by comparing similarities and differences with different alkali-ion electrochemistry. Here, using van der Waals layered Bi<sub>2</sub>Te<sub>3</sub> nanoplates as a well-defined model system, we have systematically evaluated the electrochemical performance in three distinct alkali (Li, Na, and K) ion batteries and elucidated their comparative ion storage mechanisms through the combination of in situ TEM experiments, first-principles calculations, and finite-element modeling. Noticeably, we have discovered the anomalous sodiation behavior and the associated unexpected high-rate capacity and further clarified that the origin is attributed to the unique kinetics and electrochemo-mechanical stability in Na reactions. This work provides practical implications in leveraging the fundamental understanding of alkali-ion storage mechanisms for the design of fastcharging anodes in beyond-lithium battery technologies.

#### **RESULT AND DISCUSSION**

#### Synthesis and structure of Bi<sub>2</sub>Te<sub>3</sub> nanoplates

 $Bi_2Te_3$  possesses a van der Waals-bonded layered structure with  $R\overline{3}m$  space group. Separated by the van der Waals gap, the quintuple sheets consisting of covalently bonded Bi and Te atoms are arranged along the c axis to form a hexagonal unit cell, as shown in Figure 1A. As a result of distinct cleavage energies of different crystal planes,  $Bi_2Te_3$  thermodynamically favors isotropic in-plane growth along a and b axes into a hexagonal shape. We have utilized the hydrothermal approach to synthesize single-crystalline  $Bi_2Te_3$  nanoplates with uniform hexagonal morphology, with

<sup>&</sup>lt;sup>1</sup>Department of Materials Science and Engineering, Clemson University, Clemson, SC 29634, USA

<sup>&</sup>lt;sup>2</sup>Center for Functional Nanomaterials, Brookhaven National Laboratory, Upton, NY 11973 USA

<sup>&</sup>lt;sup>3</sup>Chemistry Division, Brookhaven National Laboratory, Upton, NY 11973, USA

<sup>&</sup>lt;sup>4</sup>Lead contact

<sup>\*</sup>Correspondence: kaihe@clemson.edu https://doi.org/10.1016/j.matt.2021.01.005



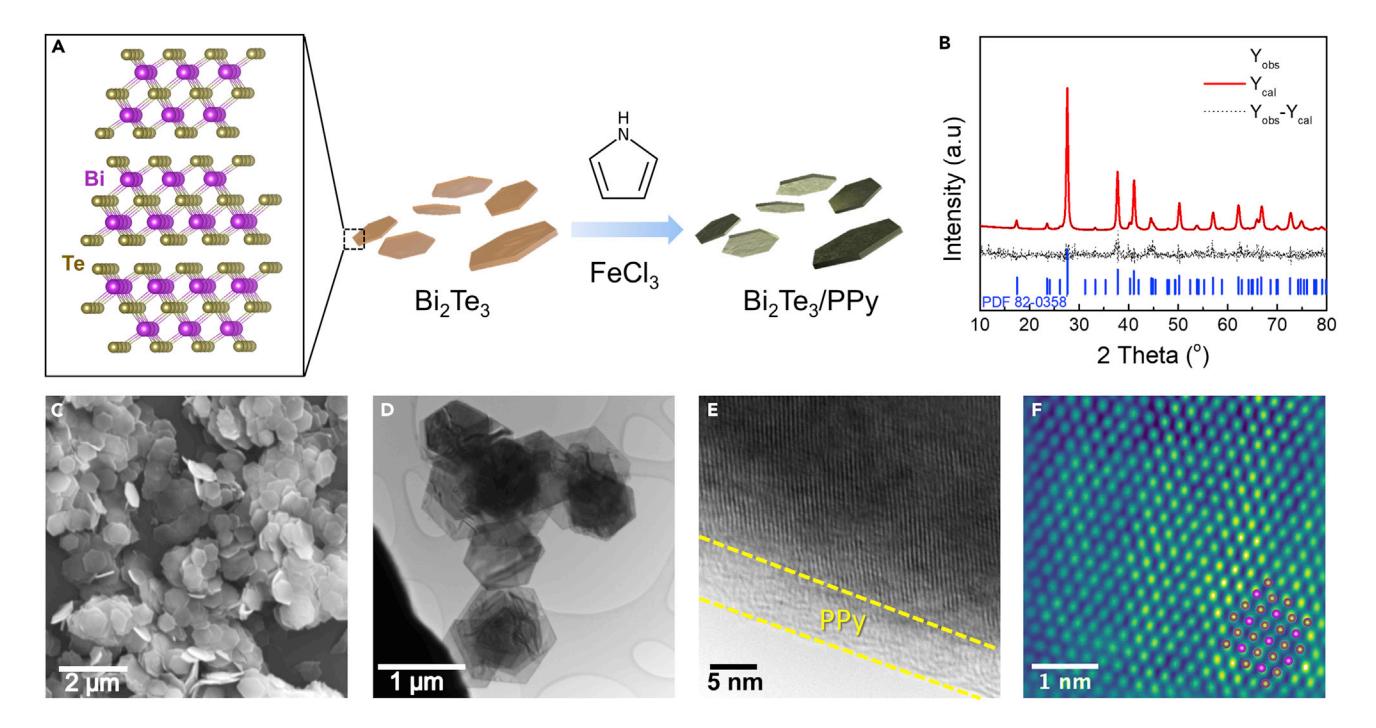


Figure 1. Synthesis and structure of Bi<sub>2</sub>Te<sub>3</sub> nanoplates

(A) Schematics showing the crystal structure and synthesis route of PPy-coated Bi<sub>2</sub>Te<sub>3</sub>.

(B-D) (B) XRD pattern, (C) SEM, and (D) TEM images of as-prepared PPy-coated Bi<sub>2</sub>Te<sub>3</sub>.

(E) HRTEM image showing a thin layer of PPy coating on the surface of Bi<sub>2</sub>Te<sub>3</sub>.

(F) Atomically resolved HAADF-STEM image of Bi<sub>2</sub>Te<sub>3</sub>.

the addition of polyvinylpyrrolidone (PVP) to enhance better monodispersity and homogeneity in size and thickness. Surface coating is an effective method to suppress the volume change and stabilize the solid electrolyte interface (SEI) layer of electrode materials during the alkali-ion insertion/extraction process in batteries. Here, we coat a thin conductive layer of polypyrrole (PPy) via in situ polymerization of pyrrole monomer on the surface of  $Bi_2Te_3$  nanoplates. Such surface coating does not affect the high purity and crystallinity of  $Bi_2Te_3$  nanoplates as confirmed by X-ray diffraction (XRD) (Figure 1B), which identifies all characteristic peaks of  $Bi_2Te_3$  without impurity. As illustrated in SEM and TEM images, the synthesized  $Bi_2Te_3$ / PPy maintains the hexagonal morphology with a uniform lateral size and ultrathin thickness (Figures 1C and 1D). A uniform PPy layer with a thickness of  $\sim 6$  nm can be clearly observed by high-resolution TEM (HRTEM) at the edge of  $Bi_2Te_3$  nanoplate (Figure 1E). Furthermore, an atomically resolved high-angle annular dark-field (HAADF) scanning TEM (STEM) image (Figure 1F) verifies the (001) basal plane consisting of Bi and Te atoms consistent with the atomic model.

#### Electrochemical performance of Bi<sub>2</sub>Te<sub>3</sub>

We have tested the electrochemical performance of bare and PPy-coated Bi $_2$ Te $_3$  in alkali-ion (Li, Na, and K) half-cells, and the results are shown in Figures 2 and S1. In the initial cycle, both Bi $_2$ Te $_3$  and Bi $_2$ Te $_3$ /PPy delivered a similar reversible Li and Na storage capacity (422 mAh g $^{-1}$  for LIBs and 406 mAh g $^{-1}$  for NIBs at 0.1 A g $^{-1}$ ), slightly higher than the theoretical capacity of Bi $_2$ Te $_3$  (402 mAh g $^{-1}$ ), whereas the K storage capacity is much lower (341 mAh g $^{-1}$ ) even at a low current density of 0.05 A g $^{-1}$ . This indicates full Li and Na storage but incomplete K storage for Bi $_2$ Te $_3$  anodes through a combination of conversion and alloying reactions. Despite the higher capacity from conversion and alloying reactions, the large volume change





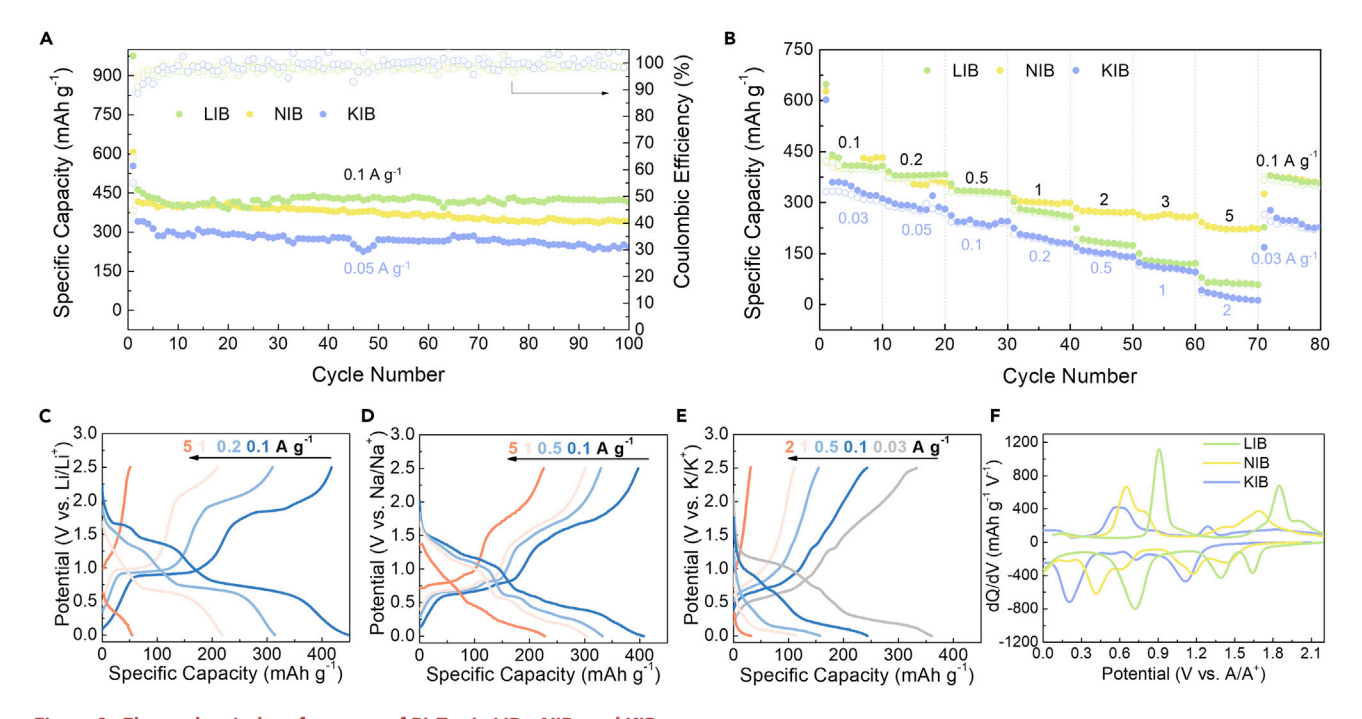


Figure 2. Electrochemical performance of  $Bi_2Te_3$  in LIBs, NIBs and KIBs (A) Cyclic, and (B) rate performance of  $Bi_2Te_3$ /PPy anodes in LIBs, NIBs and KIBs. Charge/discharge voltage profiles at various rates in (C) LIBs, (D) NIBs, and (E) KIBs, with (F) the corresponding  $d\Omega/dV$  curves.

arising from multistep phase transformations may severely deteriorate the cyclic stability<sup>38</sup> and lead to a rapid capacity decay of bare Bi<sub>2</sub>Te<sub>3</sub> anodes in all three cases (Figure S1A). It is interesting to note that the bare Bi<sub>2</sub>Te<sub>3</sub> anode retains its stability after the first 30 cycles of capacity decay in NIBs and KIBs, possibly due to the buffering effect arising from the Na- or K-telluride matrix formed through the conversion reaction that endows stable and reversible alloying reaction between Bi and Na<sup>+</sup>/K<sup>+</sup> ions.<sup>39</sup> The PPy coating can largely suppress the capacity fade and lead to the improved cyclic stability of Bi<sub>2</sub>Te<sub>3</sub>/PPy with 99%, 83%, and 71% capacity retention after 100 cycles for LIBs, NIBs, and KIBs, respectively. The largely improved cyclability is mainly attributed to the structural stability of Bi<sub>2</sub>Te<sub>3</sub>/PPy electrodes as confirmed by ex situ TEM characterization (Figure S2), in which the crystallinity of Bi<sub>2</sub>Te<sub>3</sub>/PPy is retained and no agglomeration is formed, despite the original hexagonal-shaped nanoplates being broken into smaller pieces. The rate performances of Bi<sub>2</sub>Te<sub>3</sub>/PPy in LIBs, NIBs, and KIBs are also tested (Figure 2B) and the corresponding charge/discharge voltage profiles (Figures 2C-2E) exhibit two major plateaus associated with conversion and alloying reactions, although the sluggish kinetics of K transport make them less prominent than the Li and Na counterparts. Despite the slight capacity loss due to the increasing polarization at high rates, the overall rate capability of PPy-coated Bi<sub>2</sub>Te<sub>3</sub> is significantly better than that of uncoated Bi<sub>2</sub>Te<sub>3</sub> (Figure S1B). It is worth noting that Bi<sub>2</sub>Te<sub>3</sub>/PPy in NIBs shows exceptional rate performance, especially at current densities higher than 1A g<sup>-1</sup>, and maintains the capacity of 231 mAh  $g^{-1}$  at the current density of 5 A  $g^{-1}$ . This anomalous rate capability in Na electrochemistry has also previously been reported in layered metal chalcogenide electrodes, <sup>20,21,24</sup> but the origin remains elusive.

To further elucidate the difference in alkali-ion transport kinetics in  $Bi_2Te_3$ , we have conducted various electrochemical analyses. The differential capacity (dQ/dV) curves for Li, Na, and K electrochemical reactions are plotted and compared in





Figure 2F. According to previous reports on other similar metal chalcogenide anodes, 16,20,21 the peaks within 0-1 V are ascribed to alloying reactions, while the peaks higher than 1 V are mainly contributed by conversion reactions. The cathodic and anodic peaks of LIB and NIB curves are symmetric, implying fully reversible conversion and alloying reactions consistent with the charge/discharge tests. The dQ/ dV curve for KIB shows cathodic peaks more pronounced than the corresponding anodic peaks, especially for the conversion reaction, indicating the difficulty in fully reversible K conversion reactions. The irreversible capacity loss in KIBs is attributed to the sluggish potassiation kinetics, which can be quantitatively evaluated by the diffusion coefficient of K<sup>+</sup> ions in Bi<sub>2</sub>Te<sub>3</sub>. We measured the diffusion coefficients of Li<sup>+</sup>, Na<sup>+</sup>, and K<sup>+</sup> ions in Bi<sub>2</sub>Te<sub>3</sub> by galvanostatic intermittent titration technique (GITT). 40 The overpotentials of KIBs are much larger than those of LIBs and NIBs according to the measured voltage profiles (Figure S3), but their diffusion coefficients calculated from GITT tests are essentially similar to those during alloying reactions in LIBs and NIBs. On the contrary, diffusion coefficients of Na<sup>+</sup> during the conversion reaction in NIBs are higher than those of LIBs and KIBs, which is consistent with the better rate performance of NIBs than the LIB and KIB counterparts (Figure 2B) and manifests the significant role of conversion kinetics in determining the rate capability.

#### In situ lithiation, sodiation, and potassiation

We conducted in situ TEM to unveil the similarity and difference in reaction mechanisms between lithiation, sodiation, and potassiation, and to specifically elucidate the origin of anomalous Na electrochemistry. It is expected that the electrochemical reaction between Bi<sub>2</sub>Te<sub>3</sub> and alkali metals undergoes conversion and alloying processes with possibly intercalation at the beginning, although the conversion stage is predominant. 41 In situ TEM based on the open-cell configuration has demonstrated its ability to offer unprecedented spatial resolution and ample chemical information that enables a comprehensive understanding of battery reaction mechanisms. 42 Here, we construct open cells for in situ TEM experiments that utilize monodispersed Bi<sub>2</sub>Te<sub>3</sub> nanoplates as the working electrode and native oxide solid electrolyte covered alkali metals as the counter electrode to allow quantitative analysis of structure, morphology, and phase evolutions upon electrochemical discharge reactions. 17,20,43 The time-sequential TEM/STEM images of dynamic evolutions during in situ lithiation, sodiation, and potassiation are displayed in Figure 3 (raw images are shown in Figure S4 with the coloring algorithm shown in Figure S5), which are representatively selected from original videos (Videos S1, S2, and S3) recorded in real time. It is obvious that both lithiation and sodiation processes similarly undergo a conversion-dominant reaction pathway in which the pristine Bi<sub>2</sub>Te<sub>3</sub> single crystals transform into ultrafine metallic Bi nanoparticles uniformly dispersed in the amorphous alkali-metal telluride (a-Li<sub>x</sub>Te or a-Na<sub>x</sub>Te where  $x \approx 2$ ) matrix, forming a clear reaction front between pristine and conversion regions. The reaction front continues moving from the alkali-metal contact area toward the far end of Bi<sub>2</sub>Te<sub>3</sub> nanoplate. along with the diffusion of alkali ions. The lithiation reaction front takes  $\sim$ 50 s to complete the whole conversion reaction, leading to the corresponding propagation speed of  $\sim 15.2$  nm s<sup>-1</sup> (Figure 3A). In contrast, the sodiation process shows unexpected better kinetics than lithiation. From an observation in the midst of sodiation (Figure 3B), it takes  $\sim$ 25 s to finish the entire conversion reaction of the remaining nanoplate with a faster propagation speed of  $\sim$ 28.2 nm s<sup>-1</sup>. The statistics of propagation speed from more in situ experiments are given in Figure S6. This higher sodiation speed is consistent with the better performance in rate testing (Figure 2B) and GITT measurement (Figure S3) for NIBs. It is also noted that the direct conversion phase separation without the preceding intercalation reaction is distinct from



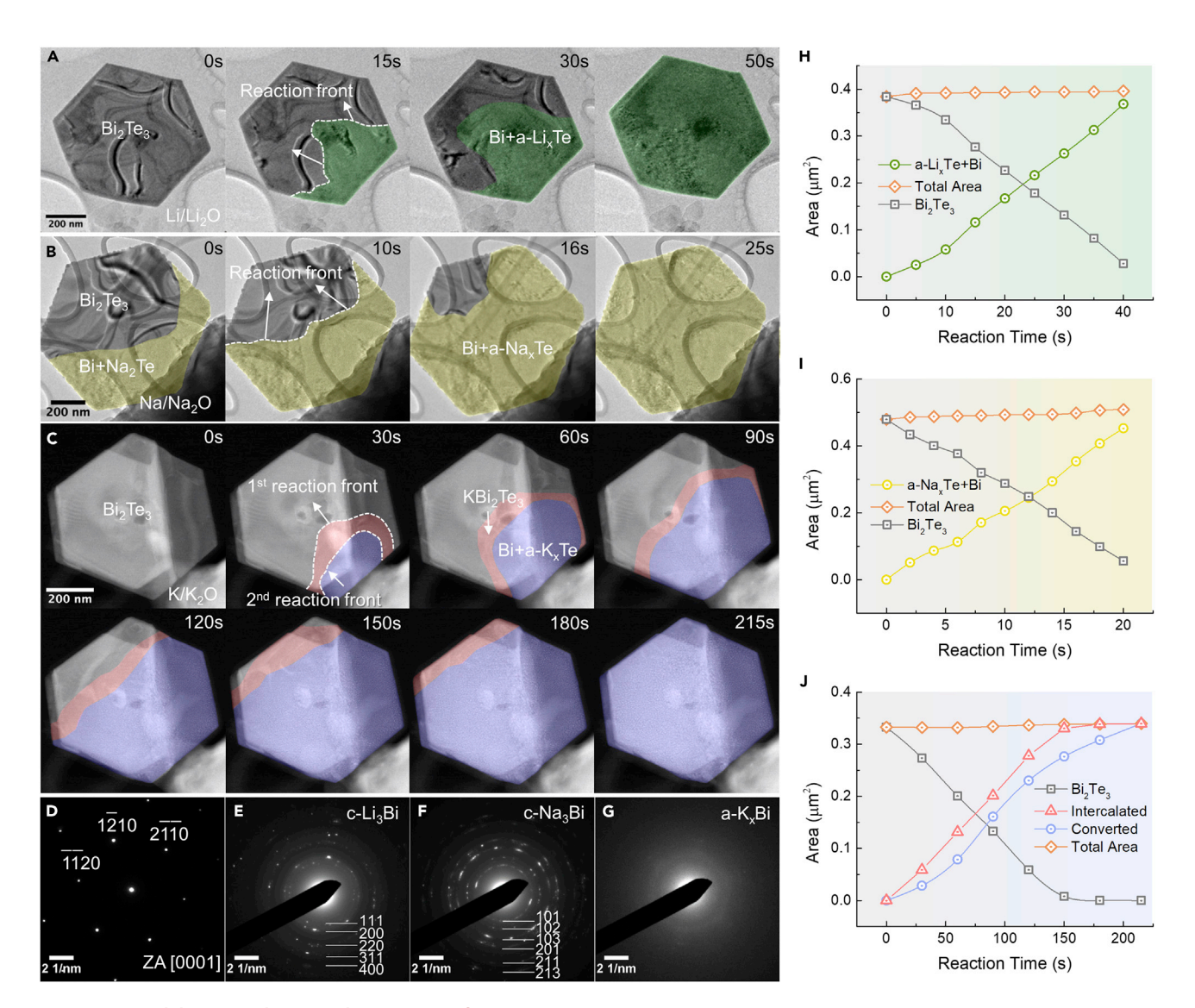


Figure 3. In situ lithiation, sodiation, and potassiation of  $\mathrm{Bi}_2\mathrm{Te}_3$ 

Sequential TEM images showing the propagation of electrochemical reaction fronts during (A) lithiation, (B) sodiation, and (C) potassiation. See also Figures S4 and S5 for processing details. SAED patterns taken from (D) pristine  $Bi_2Te_3$ , (E) fully lithiated  $Bi_2Te_3$ , (F) fully sodiated  $Bi_2Te_3$ , and (G) fully potassiated  $Bi_2Te_3$ . See also Figure S9 for index details. The reaction area as a function of time for (H) lithiation, (I) sodiation, and (J) potassiation processes.

our previous observation on the lithiation of van der Waals layered  $SnSe_2$ , <sup>44</sup> which may imply that an unusual energy barrier or unstable intercalated intermediate phase exists in the  $Bi_2Te_3$  system. We also track the propagation of reaction fronts to perform quantitative analysis of the conversion kinetics through the plot of reacted planar area change as a function of reaction time for lithiation (Figure 3H) and sodiation (Figure 3I). We find that the increase of both lithiated and sodiated areas shows linear dependence on reaction time, indicating a typical diffusion-controlled conversion reaction with a constant diffusion coefficient. <sup>45</sup> The good linearity provides extra evidence for the direct conversion reaction without any prior intercalation or side reaction that may potentially alter the diffusion coefficient.

The total areal expansion of  $Bi_2Te_3$  nanoplates before and after the full conversion reaction are measured to be only  $\sim$ 2% for lithiation and  $\sim$ 3% for sodiation, and

## Matter Article



the thickness increase is calculated to be  $\sim$ 60% for lithiation and  $\sim$ 108% for sodiation (details given in Figures S7 and S8, Tables S1 and S2), 46 which are significantly larger than the in-plane expansion, manifesting a strong anisotropic phase transformation behavior. The greater expansion along both in-plane and out-of-plane directions in sodiation is likely attributed to the larger ionic radius of Na<sup>+</sup> ions. Although KIBs share similar working principles with LIBs and NIBs, the potassiation of Bi<sub>2</sub>Te<sub>3</sub> exhibits distinct reaction pathways containing an extra reaction step compared with lithiation and sodiation. For easier tracking of two reaction fronts that simultaneously propagate within a single nanoplate, we use in situ STEM imaging with relatively low collection angle to distinguish the Z contrast arising from the  $K^{+}$ -intercalation-induced strain during the potassiation process, <sup>47,48</sup> as shown in Figure 3C (also see Video S3). For better visualization, false colors are overlaid onto STEM images to illustrate two reaction fronts. The potassiation of Bi<sub>2</sub>Te<sub>3</sub> begins with the intercalation of K<sup>+</sup> ions, followed by a conversion reaction to form Bi and a-K<sub>x</sub>Te ( $x \approx 2$ ), resulting in three regions: i.e., pristine Bi<sub>2</sub>Te<sub>3</sub>, K<sup>+</sup>-intercalated Bi<sub>2</sub>Te<sub>3</sub> (red), and K<sup>+</sup>-converted Bi+a-K<sub>x</sub>Te (blue). The coexisting intercalation and conversion regions are bounded with two reaction fronts, which propagate consecutively until the full conversion is completed. By measuring the area change of three phases, we find a linear dependence of intercalated area on reaction time (Figure 3J), indicating a diffusioncontrolled K<sup>+</sup> intercalation. However, in contrast to Li<sup>+</sup> and Na<sup>+</sup> conversions, K<sup>+</sup> conversion follows the Boltzmann sigmoidal dependence on reaction time, which is likely due to the local transport kinetics significantly altered by the initial intercalation reaction. We can infer that the initial acceleration of the conversion rate is resulted from the dramatically enhanced electrical conductivity of K<sup>+</sup>-intercalated Bi<sub>2</sub>Te<sub>3</sub> due to the topological insulator to conductor transition (Figure S12). After a prolonged period of conversion, the original conductive network of K<sup>+</sup>-intercalated Bi<sub>2</sub>Te<sub>3</sub> is replaced by the newly formed a-K<sub>x</sub>Te, which has a much lower electrical conductivity, leading to the slowdown of the conversion reaction. The overall potassiation rate and the corresponding volume change are also measured and compared with those for lithiation and sodiation. The potassiation propagates at a rate of 3.2 nm s<sup>-1</sup> with a total in-plane expansion of  $\sim$ 3%. The potassiation reaction speed is much slower than that of lithiation and sodiation, indicating the lowest reaction kinetics among the three electrochemical processes. It is also interesting to note that the reaction front exhibits a convex geometry in lithiation and potassiation but a concave geometry in sodiation, which may be attributed to the significantly fast Na<sup>+</sup> diffusion on the surface of carbon film, as deduced from the first-principles calculation (Figure S16).

In addition to the structural evolution, we have also examined the phase transformation and confirmed the final reaction products using selected area electron diffraction (SAED) and HRTEM. Figures 3D–3G shows SAED patterns of pristine Bi<sub>2</sub>Te<sub>3</sub>, and reaction products after lithiation, sodiation, and potassiation, respectively. The pristine single-crystalline hexagonal pattern (Figure 3D) transfers into polycrystalline ring patterns (Figures 3E and 3F), which are indexed to crystalline Li<sub>3</sub>Bi and Na<sub>3</sub>Bi after complete lithiation and sodiation (Figure S9), indicating that the alloying reaction takes place after the conversion reaction following Equations 1, 2, 3, and 4:

$$Bi_2Te_3 + 3xLi^+ + 6e^- \rightarrow 2Bi + 3Li_xTe (x \approx 2)$$
 (Equation 1)

$$Bi + 3Li^{+} + 3e^{-} \rightarrow Li_{3}Bi$$
 (Equation 2)





$$Bi_2Te_3 + 3xNa^+ + 6e^- \rightarrow 2Bi + 3Na_xTe (x \approx 2)$$
 (Equation 3)

$$Bi + 3Na^+ + 3e^- \rightarrow Na_3Bi$$
 (Equation 4)

After prolonged *in situ* lithiation, the final morphology becomes enormous  $Li_3Bi$  alloy nanoparticles uniformly dispersed inside an amorphous  $Li_xTe$  matrix (Figures S10A and D), which is beneficial for stable cycling of  $Bi_2Te_3$  in LIBs.<sup>49,50</sup> Similar morphology is also confirmed to contain nanocrystalline  $Na_3Bi$  and amorphous  $Na_xTe$  after complete sodiation (Figures S10B and E).

Unlike lithiation and sodiation, the theoretical completion of potassiation is difficult to achieve even after a prolonged time. The SAED pattern after potassiation for 780 s is shown in Figure 3G, which still displays weakened but well-retained hexagonal characteristics inherited from the original  $Bi_2Te_3$  lattice. In fact, this inherent hexagonal symmetry is preserved during the entire potassiation process, although a slight increase (~2%) of lattice spacing can be identified upon K<sup>+</sup> ion insertion (Figure S11), which is in agreement with the 3% in-plane expansion measured from *in situ* imaging (Figure 3C). It is also noted that no diffraction spots or rings corresponding to crystalline K-Bi alloys is observed in Figure 3G, implying the amorphous nature of final potassiation products. It further indicates that the dispersive nanoparticles with an average size of ~8 nm (Figures S10C and S10F) may likely be amorphous intermediate  $K_yBi$  (y < 3) alloys. The extremely slow and incomplete alloying reaction is a direct reflection of the sluggish kinetics of potassiation, which further accounts for the relatively low reversible K storage capacity.

#### Mechanism of alkali-ion reaction with Bi<sub>2</sub>Te<sub>3</sub>

In situ TEM experiments on alkali-ion reactions with  $Bi_2Te_3$  have unveiled several unique phase transformation behaviors as follows: (1) only potassiation undergoes the intercalation prior to the conversion reaction, whereas the direct conversion reaction takes place for lithiation and sodiation; (2) the alloying reactions of lithiation and sodiation are complete, whereas potassiation shows incomplete alloying reaction with the formation of intermediate  $K_yBi$  alloys; (3) sodiation unexpectedly exhibits the highest kinetics among three alkali-ion reactions; (4) the volume expansion is highly anisotropic along in-plane and out-of-plane directions for lithiation, sodiation, and potassiation. To further elucidate the origin of these unique but unclarified phenomena, we conduct theoretical simulations using a combination of first-principles calculations and finite-element analysis.

We have searched all possible phases that may occur during intercalation, conversion, and alloying reactions for each alkali-Bi $_2$ Te $_3$  system. It is worth noting that the intercalation reaction involves the occupation of alkali ions in between the quintuple layers of Bi $_2$ Te $_3$ . We conducted an enumeration of likely arrangements of alkali ions at all vacancy sites and calculate the density functional theory energies of all superstructures to find the thermodynamically stable intermediate phases. The voltage profiles can then be calculated according to Equation 5, where V is the voltage, A represents the alkali metal, E is the energy obtained from the DFT calculation, X is the stoichiometric number of alkali ions, and E is the Faraday constant.

$$V \approx -\frac{E(A_{x1}Bi_2Te_3) - E(A_{x2}Bi_2Te_3) - (x_1 - x_2)E(A)}{(x_1 - x_2)F}$$
 (Equation 5)



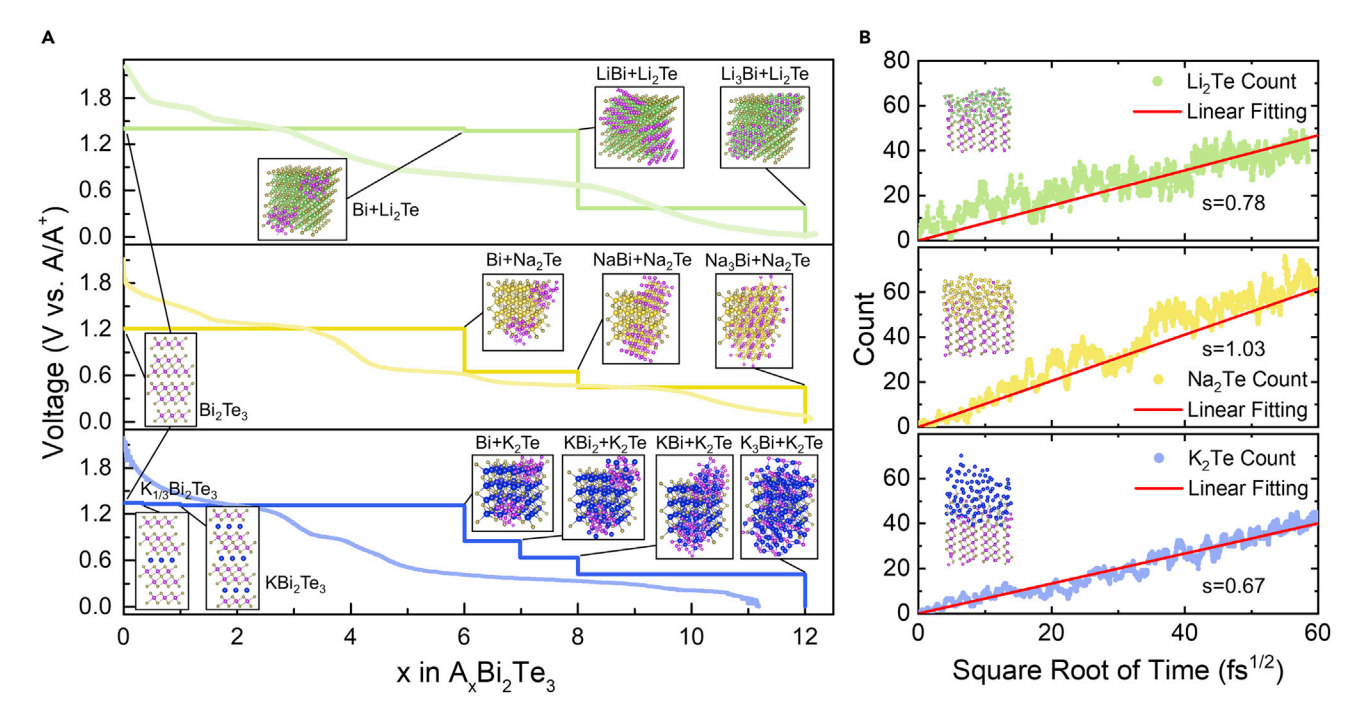


Figure 4. First-principles calculation of reaction pathways and kinetics

(A) Experimental equilibrium discharge curves from GITT measurements along with the DFT calculated voltage profiles of  $Bi_2Te_3$  against Li, Na, and K, respectively.

(B) Statistics of the reaction product of  $A_2$ Te (A = Li, Na, K) as a function of simulation time with insets showing the snapshots of AIMD simulations on conversion reaction between  $Bi_2$ Te<sub>3</sub> and Li, Na, and K. The red lines are linear fitting with the slope proportional to the reaction speed.

Figure 4A shows the calculated and measured voltage profiles of alkali-ion insertion into  $Bi_2Te_3$ . For lithiation and sodiation, the conversion reactions from  $Bi_2Te_3$  to Bi +Li<sub>2</sub>Te/Na<sub>2</sub>Te are energetically more favorable than the intercalation reaction. As a result, no intercalation reaction can take place during lithiation and sodiation, which explains the single reaction front observed by in situ TEM. On the contrary, we have identified two stable phases for K<sup>+</sup> intercalation; i.e., K<sub>1/3</sub>Bi<sub>2</sub>Te<sub>3</sub> and KBi<sub>2</sub>Te<sub>3</sub> (Table S3). The formation of those phases leads to an initial intercalation reaction prior to the conversion, which is consistent with the observation of double reaction fronts during potassiation. Despite the higher calculated voltages than the measured values due to inevitable polarizations, the calculation of voltage profiles generally shows a good agreement with the experimental curves, which further validates our suggested phase transformation pathways. In addition to the difference of intercalation, the alloying reaction during potassiation proceeds through three different K-Bi alloy phases, while only two Li-Bi and Na-Bi alloy phases are identified for the lithiation and sodiation. More intermediate phases will pose severe enthalpy and entropy penalties that hinder the complete alloying reactions, which in turn causes the irreversible loss of capacity in KIB cells and the absence of crystalline K<sub>3</sub>Bi alloys during in situ TEM observation. Based on the DFT calculation and in situ TEM observation, the potassiation of Bi<sub>2</sub>Te<sub>3</sub> follows the route described by Equations 6, 7, and 8.

$$Bi_2Te_3 + K^+ + e^- \rightarrow KBi_2Te_3$$
 (Equation 6)

$$KBi_2Te_3 + (3x-1)K^+ + 5e^- \rightarrow 2Bi + 3K_xTe (x \approx 2)$$
 (Equation 7)



Bi + 
$$yK^{+}$$
 +  $ye^{-} \rightarrow K_{y}Bi$  (0 <  $y \le 3$ ) (Equation 8)

We have further accessed the kinetics of alkali-ion reactions by DFT calculation and ab initio molecular dynamics (AIMD) simulation. DFT results suggest that the diffusion paths of Li<sup>+</sup>, Na<sup>+</sup>, and K<sup>+</sup> in Bi<sub>2</sub>Te<sub>3</sub> are found to be essentially identical to each other, but the diffusion barriers are proportional to their ion radius; i.e., 0.45 eV for Li<sup>+</sup>, 0.74 eV for Na<sup>+</sup>, and 0.92 eV for K<sup>+</sup> (Figure S13), possibly due to the enhancement of electrostatic interactions with neighboring Te atoms as increase of ion radius. The monotonic increase of thermodynamic barriers for Li<sup>+</sup>, Na<sup>+</sup>, and K<sup>+</sup> accounts for the sluggish reaction kinetics for potassiation, but it does not accord with the controversy over the anomalous high-rate performance of sodiation. It is also worth noting that the DFT calculation of diffusion barrier based on the alkaliion diffusion in the pristine Bi<sub>2</sub>Te<sub>3</sub> lattice is different from the realistic lithiation and sodiation, where direct conversion occurs at the initial stage. This discrepancy may hinder an accurate understanding so that we also performed AIMD simulations to fully reveal the origin of the anomalous fast sodiation mechanism in Bi<sub>2</sub>Te<sub>3</sub>. AIMD simulations generate dynamic trajectories of all involved atoms in an accurate and unbiased manner to precisely describe the microscopic mechanism for alkali-ion reactions and closely resemble the experimental observations, 53 as shown in Figures 4B and S14. With the increasing simulation time, spontaneous conversion reactions between alkali ions and Bi<sub>2</sub>Te<sub>3</sub> crystals occur, leading to the emergence of Binanoclusters embedded in the amorphous  $A_2$ Te (A = Li, Na, K) matrix along with the progression of phase separation boundaries (Figure S14), which is consistent with in situ TEM observations. We use the quantity of newly formed reaction product A<sub>2</sub>Te as a function of the simulation time (Figure S15) to quantify the reaction speed and kinetics. In this AIMD model, the progression of phase separation has only one degree of freedom along the b axis since periodic boundary conditions are applied to the other two axes. Therefore, the increasing number of A<sub>2</sub>Te abides by Fick's law of diffusion and follows a linear relationship with the square root of the simulation time (Figure 4B), which is consistent with the diffusion-controlled conversion reactions observed by in situ TEM. More importantly, the reaction speed measured as the slope of the linear fitting indicates the highest value for sodiation among all three processes. This phenomenon confirms the crucial role of phase separation kinetics and implies that the anomalous high-rate performance in NIBs is dictated by the rapid propagation of phase separation interfaces rather than the diffusion barrier in Bi<sub>2</sub>Te<sub>3</sub> lattices. From the thermodynamic standpoint, a typical conversion-type phase transformation induces the total Gibbs free energy change ( $\Delta G$ ) consisting of energy changes in chemical potential ( $\Delta G_{chem}$ ), strain accommodation energy  $(\Delta G_{strain})$ , and interfacial energy  $(\Delta G_{int})$ , as described by Equation 9:<sup>54</sup>

$$\Delta G = \Delta G_{chem} + \Delta G_{strain} + \Delta G_{int}$$
 (Equation 9)

It is obvious that  $\Delta G$  is the AIMD enthalpy difference before and after the conversion phase separation and  $\Delta G_{chem}$  is represented by the DFT energy difference between the Bi<sub>2</sub>Te<sub>3</sub> crystal and the reaction products of A<sub>2</sub>Te and Bi. Consequently, the sum of strain accommodation and interfacial energy changes ( $\Delta G_{strain+int}$ ), which is otherwise difficult to directly calculate, can be obtained as the difference between  $\Delta G$  and  $\Delta G_{chem}$  (Table S4). It is interesting to note that  $\Delta G_{strain+int}$  of sodiation is not only lower than that of potassiation but also lower than the lithiation counterpart, which means the phase separation in sodiation is more favorable to proceed than the other two alkali-ion reactions due to the ease of interface formation and strain accommodation. One possible explanation for this intriguing result is that the Bi-Te bond length in Bi<sub>2</sub>Te<sub>3</sub> (3.29 Å) is closest to the Na-Te bond length (3.18 Å) compared



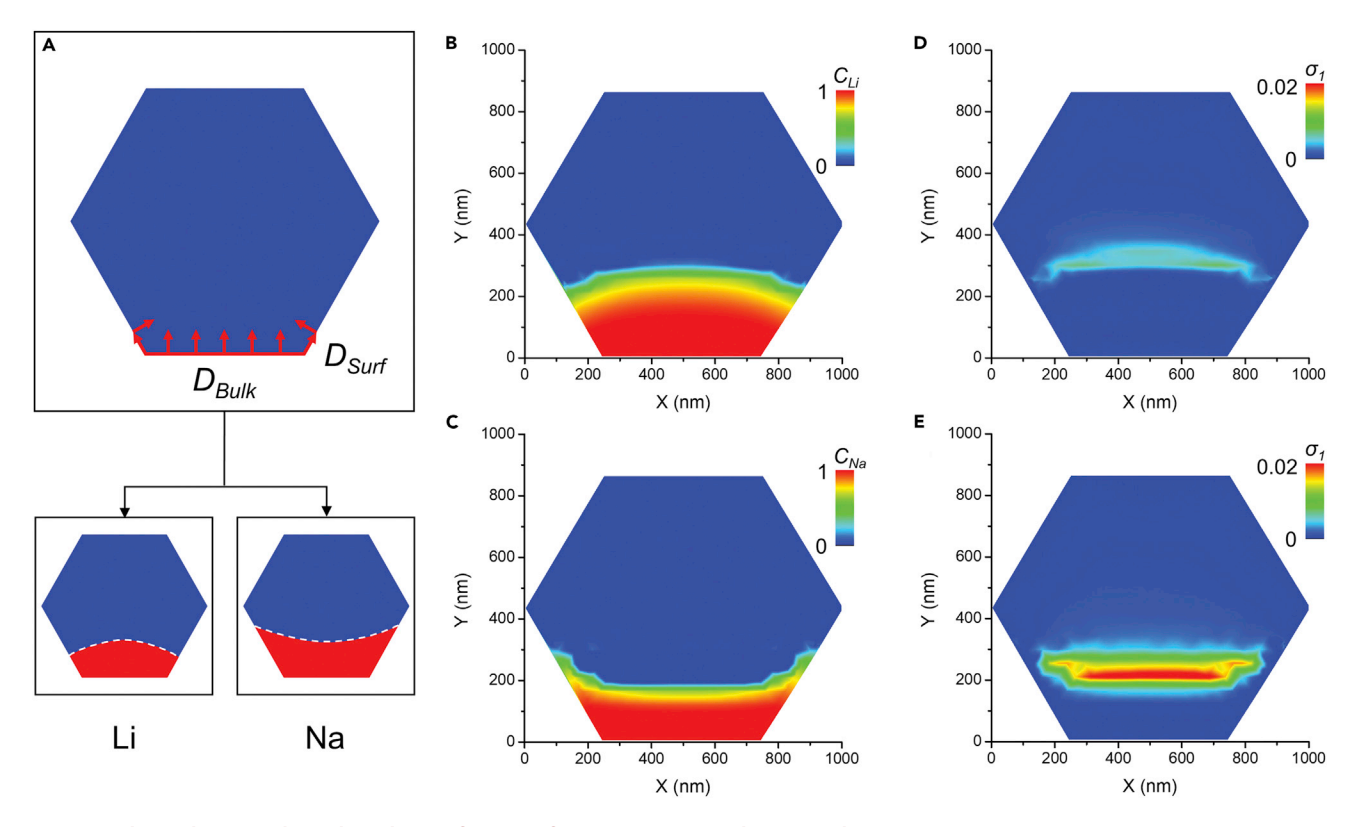


Figure 5. Electrochemo-mechanical simulation of reaction front propagation and stress evolution

(A) Schematics showing the geometry and boundary condition of the FEA model, in which a constant concentration of Li/Na is applied to the bottom edge face and the ion diffusion can proceed along bulk and surface paths to generate different reaction front geometries. The red color denotes the  $reacted\ region\ with\ full\ Li/Na\ concentration,\ the\ blue\ color\ represents\ the\ unreacted\ Bi_2Te_3\ region\ with\ zero\ Li/Na\ concentration,\ and\ the\ white\ dashed$ lines indicate the reaction fronts.

(B and C) Simulated Li and Na concentration ( $C_{Li}$  and  $C_{Na}$ ) distributions at representative states in the midst of (B) lithiation and (C) sodiation reactions, respectively. The concentrations are normalized by the maximum concentration at full lithiation or sodiation.

(D and E) Simulated maximum principal stress ( $\sigma_1$ ) distributions in representative states of (D) lithiation and (E) sodiation, corresponding to (B) and (C), respectively. The stresses are normalized by Young's modulus of Bi<sub>2</sub>Te<sub>3</sub>. FEA simulation using the point-contact boundary condition can be found in Figure S23.

with Li-Te (2.83 Å) and K-Te (3.56 Å) bonds in conversion products, which minimizes the lattice mismatch in the vicinity of the interface between converted Na<sub>2</sub>Te and unreacted  $Bi_2Te_3$ , and thus leads to low  $\Delta G_{strain+int}$ .

The stress evolution associated with the volume change upon electrochemical ion insertion has a critical effect on the reaction kinetics and mechanical integrity in alkali-ion batteries. The unique anisotropic volume change with different reaction front geometries identified by in situ TEM may lead to a distinct stress configuration that is responsible for the anomalous sodiation behavior. We performed the electrochemo-mechanical modeling using finite-element analysis (FEA) to simulate the ion diffusion-induced reaction front propagation and the volume expansion-generated stress distribution. Since potassiation has a different reaction pathway and significantly low reaction kinetics, we only carried out the FEA simulation for lithiation and sodiation to elucidate the origin of fast sodiation kinetics. We built a threedimensional (3D) model for the hexagonal nanoplate and applied a constant concentration boundary condition to the bottom edge face to allow Li or Na diffusion to proceed through both bulk and surface paths (Figure 5A). To mimic the conversion reaction, the concentration-dependent diffusivity is used,  $^{13,55}$  and the initial





bulk and surface diffusion coefficients are obtained from AIMD simulations (details are described in Figure S17). The geometry of reaction fronts is related to the relative diffusion speed between surface and bulk paths. The time-dependent FEA captures the geometry of the reaction front and its evolution trajectory throughout the lithiation and sodiation processes, as represented by the concentration isosurface shown in Figure 5 B and C. Both convex and concave geometries are reproduced for the reaction fronts in lithiation and sodiation, respectively, which are consistent with in situ TEM observations. The reacted area as a function of time measured from time-dependent simulations (Videos S4 and S5) shows linear dependence for both lithiation and sodiation (Figure \$18), indicating sodiation speed about two times faster than lithiation, which also agrees with in situ TEM observations (Figures 3H and 31). The concentration-stress correlation can be further determined by linking the concentration-dependent volume expansion to the mechanical strain-stress relationship of Bi<sub>2</sub>Te<sub>3</sub>. The reaction-induced stress distribution corresponding to the concentration profiles in lithiation and sodiation is displayed in the plots of maximum principal stress ( $\sigma_1$ ) in Figures 5D and 5E, respectively. Three normal stresses ( $\sigma_{xx}$ ,  $\sigma_{yy}$ ,  $\sigma_{zz}$ ) in the calculated stress tensor can be found in Figure S19. We note that both lithiation and sodiation generate the tensile stress, which is spatially concentrated at the reaction front; however, the tensile stress associated with the concave reaction front of sodiation is considerably higher than that with the convex reaction front of lithiation. The generated stress will facilitate the alkali-ion diffusion in the continued conversion reaction; therefore, the propagation of the reaction front will be more significantly promoted in sodiation than lithiation. From the standpoint of mechanical integrity, the geometry of the reaction front also has a direct impact on the fracture of unreacted Bi<sub>2</sub>Te<sub>3</sub> nanoplate. The convex reaction front generates sharp corners in the unreacted region and the associated stress concentrations can drive fracture at those sharp corners, whereas the concave reaction front makes a rounded border of the unreacted region that enhances its tolerance to fracture and alleviates potential mechanical failure during prolonged cycling. A similar shape effect has also been reported previously in the sodiation of FeS<sub>2</sub>.<sup>13</sup> It is worth noting that the abovementioned propagation kinetics and the geometry of reaction front are almost independent of the planar size, thickness, and contact condition in the FEA simulation, while the reaction-induced stress may affect larger areas for thicker nanoplates due to the increasing difficulty in stress relief when the geometry is gradually changed from 2D to 3D, as shown in Figures S20-S23. The FEA modeling manifests the critical role of reaction front geometry in the superior sodiation kinetics and stability. Overall, the first-principles and finiteelement simulations jointly provide insights into the origin of anomalous high-rate performance in the Na storage mechanism.

#### **Conclusions**

This study systematically compared the electrochemical reactions of three alkalimetal ions (i.e., Li<sup>+</sup>, Na<sup>+</sup>, and K<sup>+</sup>) with 2D van der Waals layered Bi<sub>2</sub>Te<sub>3</sub> anodes. The alkali-ion storage mechanism of Bi<sub>2</sub>Te<sub>3</sub> was elucidated by combining electrochemical analysis with *in situ* TEM, first-principles calculation, and finite-element modeling. The Bi<sub>2</sub>Te<sub>3</sub> anode in the form of hexagonal nanoplates exhibits reversible electrochemical capacity and good cyclic stability in LIB, NIB, and KIB settings, among which Na anomalously shows the highest rate capability. The reaction pathways and related phase transformations directly identified by *in situ* TEM illustrate that both lithiation and sodiation experience consecutive conversion and alloying reactions, whereas an additional intercalation reaction occurs at the beginning of potassiation, making it a three-step intercalation-conversion-alloying process. The quantitative measurements of reaction front propagation indicate faster reaction





kinetics for sodiation than for lithiation and potassiation, which is counterintuitive to the conventional wisdom of sluggish sodium reaction. The AIMD and FEA simulations were jointly employed to elucidate the origin of anomalous sodiation behavior. AIMD reveals that the lower interfacial strain accommodation energy difference between the pristine  $\mathrm{Bi}_2\mathrm{Te}_3$  and its Na-conversion products facilitates the high kinetics in sodiation, while FEA unveils that the unique concave geometry of the sodiation reaction front makes the stress evolution in favor of promoting continued sodiation and mitigating mechanical fracture. These findings add essential knowledge to mechanistic understanding of alkali-ion storage mechanism in layered metal chalcogenides and offer practical guidance to the design and engineering of next-generation high-power batteries based on Na $^+$  or even larger ions. This work also suggests that the reaction kinetics and electrochemical properties of larger alkali ions should not be solely assessed by empirical implications but require precise analysis in specific scenarios.

#### **EXPERIMENTAL PROCEDURES**

#### Resource availability

#### Lead contact

Further information and requests for resources and materials should be directed to and will be fulfilled by the lead contact, Kai He (kaihe@clemson.edu).

#### Materials availability

All unique/stable reagents generated in this study are available from the lead contact without restriction.

#### Data and code availability

The published article includes all data generated or analyzed during this study.

#### Synthesis of Bi<sub>2</sub>Te<sub>3</sub> nanoplates

 $\rm Bi_2Te_3$  nanoplates were synthesized following a previous reported hydrothermal method.  $^{36}$  In a typical synthesis, 1.5 mmol of  $\rm Na_2TeO_3$  was mixed with 1 mmol of  $\rm BiCl_3$  to achieve the ratio of Te:Bi = 3:2. The mixed powder was then dissolved in 50 mL of ethylene glycol solution containing 0.4 g of NaOH and 0.5 g of PVP under constant stirring. The obtained clear solution was transferred into a Teflon-lined autoclave and kept at 180°C for 36 h. The reaction product was washed with deionized (DI) water, and  $\rm Bi_2Te_3$  nanoplates were separated from the solution by centrifugation and dried at 60°C for 12 h.

To coat a thin and uniform layer of PPy on the surface of  $Bi_2Te_3$  nanoplates, 150 mg of as-prepared  $Bi_2Te_3$  powder was first dispersed in 10 mL of DI water and then added to 10 mg of sodium dodecylbenzenesulfonate (SDBS) during sonication. The resultant dispersion was vigorously stirred for 15 min. Meanwhile, 30  $\mu$ L of pyrrole monomer was dissolved in 10 mL of ethanol, and the solution was added into the aforementioned dispersion followed by continuously stirring for 1 h. The pyrrole was polymerized by dropwise, adding 10 mL of 0.2 M FeCl $_3$  solution into the dispersion at 0°C, and the dispersion was kept stirring for another 2 h. Finally, PPy-coated  $Bi_2Te_3$  nanoplates ( $Bi_2Te_3$ /PPy) were obtained by centrifugation and washed several times with DI water followed by drying at 60°C for 12 h.

#### **Materials characterization**

The phase and crystallinity of  $Bi_2Te_3$  nanoplates was verified by the powder XRD (Rigaku Ultima IV). The structure and morphology characterization of  $Bi_2Te_3$  nanoplates were performed using SEM (Hitachi SU6600, 30 kV) and TEM (Hitachi H9500, 300 kV).





kV). The atomic structure of  $Bi_2Te_3$  nanoplates was characterized by aberration-corrected HAADF-STEM (Hitachi HD2700C, 200 kV).

#### In situ TEM experiments

In situ TEM experiments were conducted using JEOL 2100F TEM operated at 200 kV in either TEM or STEM mode. Bi<sub>2</sub>Te<sub>3</sub> nanoplates were dispersed onto a TEM halfgrid and loaded into the Nanofactory TEM-STM holder, in which a piezo-driven tungsten probe coated with a layer of alkali metal (Li, Na, K) can approach the half-grid and contact with the desired Bi<sub>2</sub>Te<sub>3</sub> nanoplates. All the operations involving alkali metals were performed inside an Ar-filled glovebox. The holder was transferred into the TEM column using a glove bag with minimal exposure to air to form a native oxide layer on the alkali-metal surface as the solid electrolyte. During in situ TEM observation, the tungsten probe was carefully manipulated to allow the alkali-metal contact with a single Bi<sub>2</sub>Te<sub>3</sub> nanoplate. A negative bias of -0.5 V was applied to the half-grid with respect to the probe to drive the diffusion of alkali ions toward Bi<sub>2</sub>Te<sub>3</sub> nanoplates and initiate in situ electrochemical reactions, which were recorded in real time. To eliminate unnecessary side effects arising from the electron radiation damage or electron-beam-induced reaction, the controlled electron dose rate was used and the electron beam was blanked during the electrochemical reaction except for recording images or videos. Control experiments were also performed by exposing pristine and reacted Bi<sub>2</sub>Te<sub>3</sub> under the same electron dose for a prolonged time, with no obvious change observed.

#### **Electrochemical tests**

The electrochemical performance of bare and PPy-coated Bi<sub>2</sub>Te<sub>3</sub> was tested using a coin-cell configuration. Typically, the active materials were mixed with super P, carboxymethyl cellulose (CMC), and polyacrylic acid (PAA) in a weight ratio of 60:20:15:5. The mixed powder was dispersed in DI water and stirred for 18 h to form a uniform slurry. The slurry was then coated onto a copper foil and fully dried in a vacuum oven at 80°C, from which disks with a diameter of 15 mm were cut. The typical mass loading was  $\sim$ 2 mg cm $^{-2}$ . The electrode disks were then assembled into CR2032 coin cells inside an Ar-filled glovebox. For LIBs, commercially available Li foil was used as the counter electrode, and Celgard 2400 was used as the separator. The electrolyte was made of 1 M LiPF<sub>6</sub> in ethylene carbonate/dimethyl carbonate (EC/DMC, 3:7 vol %). For NIBs, freshly cut Na disks were used as counter electrode, and glass fiber mats (Whatman GF/D) were used as separator. The electrolyte was made of 1 M NaClO<sub>4</sub> dissolved in propylene carbonate/ethylene carbonate (PC/EC, 1:1 vol %) with 5% fluoroethylene carbonate (FEC) additive. For KIBs, freshly cut K disks were assembled into symmetric cells and cycled at a current density of  $0.1 \,\mathrm{mA}\,\mathrm{cm}^{-2}$  with a cutoff capacity of  $1 \,\mathrm{mAh}\,\mathrm{cm}^{-2}$  for five times to alleviate the polarization arising from the K plating/stripping. The cycled K disks were then used as counter electrode for electrochemical tests of Bi<sub>2</sub>Te<sub>3</sub> and Bi<sub>2</sub>Te<sub>3</sub>/PPy. The electrolyte comprises 1 M potassium bis(fluorosulfonyl)imide (KFSI) dissolved in diethyl carbonate/ethylene carbonate (DEC/EC, 1:1 vol %). Galvanostatic charge/ discharge method was used for the evaluation of cyclic and rate performance of batteries and the voltage range was set to 0-2.5 V. To study the diffusion properties, GITT was employed at a voltage range of 0-2.5 V with a current pulse of 10 mA  $g^{-1}$  for 10 min and relaxation time of 30 min.

#### Simulation and modeling

DFT calculations were carried out under the general gradient approximation with the Perdew-Burke-Ernzerhof (PBE) functionals<sup>56</sup> and projector augmented wave (PAW) pseudopotentials<sup>57</sup> using the Quantum Espresso code.<sup>58</sup> The kinetic cutoff for plane





waves was set at 600 eV for calculations containing Li atoms, while 520 eV was used for all other cases. Monkhorst-Pack meshes with spacings smaller than 0.1  $\mathring{A}^{-1}$  were used to sample the reciprocal space.  $^{59}$  The convergence criterion was  $10^{-6}$  eV for the electron self-consistent calculations and  $10^{-2}$  eV  $\mathring{A}^{-1}$  for the Hellmann-Feynman forces during the relaxation of ions. The diffusion barriers were calculated by the climb-image nudged elastic band (NEB) method<sup>60</sup> using nine images for each calculation. The elastic tensors were calculated by applying various deformations to the unit cell followed by further structural optimizations using ab initio calculations. Such a process was automated by using the ElaStic tool<sup>61</sup> interfaced with the Quantum Espresso code. The electronic and force optimization of the ab initio MD simulation are essentially the same as the DFT calculation. A simulation box containing Bi<sub>2</sub>Te<sub>3</sub> and alkali metal (392 total atoms) was used for AIMD simulation, and the simulation was carried out at an elevated temperature of 500 K to accelerate the phase transformation and reduce the computational cost. The temperature was controlled by the Nosé-Hoover thermostat, and only gamma point was sampled throughout the AIMD simulation. The FEA was performed using COMSOL Multiphysics software to simulate the alkali-ion diffusion and the resultant stress concentration in the Bi<sub>2</sub>Te<sub>3</sub> nanoplate. All the parameters for simulations were obtained either by electrochemical measurements or DFT calculations carried out in this study. The detailed FEA setup is given in Supplemental Information.

#### SUPPLEMENTAL INFORMATION

Supplemental information can be found online at https://doi.org/10.1016/j.matt. 2021.01.005.

#### **ACKNOWLEDGMENTS**

The authors acknowledge Clemson University start-up fund and generous allotment of computing time on Palmetto cluster. K.H. and J.C. were partially supported by the National Science Foundation (award no. 1929138). This research used resources of the Center for Functional Nanomaterials, which is a US DOE Office of Science Facility, at Brookhaven National Laboratory under contract no. DE-SC0012704. X.Q.Y. was supported by the Assistant Secretary for Energy Efficiency and Renewable Energy, Vehicle Technologies Office of the US Department of Energy through the Advanced Battery Materials Research (BMR) Program under contract no. DE-SC0012704.

#### **AUTHOR CONTRIBUTIONS**

J.C. and K.H. conceived the idea and designed the experiments. J.C. carried out materials synthesis; electrochemical tests; *in situ* TEM characterization; and DFT, AIMD, and FEA simulations under K.H.'s guidance. H.Z. and Z.Z. assisted with electrochemical tests and TEM measurements. S.H. and X.Q.Y. assisted with electrochemistry and *in situ* TEM experiments. J.C. and K.H. wrote the manuscript with input from all authors. K.H. supervised the project.

#### **DECLARATION OF INTERESTS**

The authors declare no competing interests.

Received: September 22, 2020 Revised: December 7, 2020 Accepted: January 4, 2021 Published: February 1, 2021



### Matter Article

#### REFERENCES

- Tarascon, J.M., and Armand, M. (2001). Issues and challenges facing rechargeable lithium batteries. Nature 414, 359–367.
- Cui, J., Yao, S., and Kim, J.K. (2017). Recent progress in rational design of anode materials for high-performance Na-ion batteries. Energy Storage Mater. 7, 64–114.
- 3. Liang, Y., and Yao, Y. (2018). Positioning organic electrode materials in the battery landscape. Joule 2, 1690–1706.
- Wu, X., Leonard, D.P., and Ji, X. (2017). Emerging non-aqueous potassium-ion batteries: challenges and opportunities. Chem. Mater. 29, 5031–5042.
- Hao, F., Chi, X., Liang, Y., Zhang, Y., Xu, R., Guo, H., Terlier, T., Dong, H., Zhao, K., Lou, J., et al. (2019). Taming active material-solid electrolyte interfaces with organic cathode for all-solid-state batteries. Joule 3, 1349–1359.
- Hu, Y., Komaba, S., Forsyth, M., Johnson, C., and Rojo, T. (2019). A new emerging technology: Na-ion batteries. Small Methods 3, 1900184.
- Yu, X., Xue, L., Goodenough, J.B., and Manthiram, A. (2020). Ambient-temperature all-solid-state sodium batteries with a laminated composite electrolyte. Adv. Funct. Mater. 31, 2002144.
- 8. Ni, J., Li, L., and Lu, J. (2018). Phosphorus: an anode of choice for sodium-ion batteries. ACS Energy Lett. 3, 1137–1144.
- Zhang, H., Hasa, I., and Passerini, S. (2018). Beyond insertion for Na-ion batteries: nanostructured alloying and conversion anode materials. Adv. Energy Mater. 8, 1702582.
- Tan, H., Chen, D., Rui, X., and Yu, Y. (2019). Peering into alloy anodes for sodium-ion batteries: current trends, challenges, and opportunities. Adv. Funct. Mater. 29, 1808745.
- Ge, P., and Fouletier, M. (1988). Electrochemical intercalation of sodium in graphite. Solid State Ion. 28, 1172–1175.
- Jian, Z., Luo, W., and Ji, X. (2015). Carbon electrodes for K-ion batteries. J. Am. Chem. Soc. 137, 11566–11569.
- Boebinger, M.G., Yeh, D., Xu, M., Miles, B.C., Wang, B., Papakyriakou, M., Lewis, J.A., Kondekar, N.P., Cortes, F.J.Q., Hwang, S., et al. (2018). Avoiding fracture in a conversion battery material through reaction with larger ions. Joule 2, 1783–1799.
- He, H., Huang, D., Gan, Q., Hao, J., Liu, S., Wu, Z., Pang, W.K., Johannessen, B., Tang, Y., Luo, J.L., et al. (2019). Anion vacancies regulating endows MoSSe with fast and stable potassium ion storage. ACS Nano 13, 11843–11852.
- 15. Yao, S., Cui, J., Huang, J.Q., Lu, Z., Deng, Y., Chong, W.G., et al. (2018). Novel 2D Sb<sub>2</sub>S<sub>3</sub> nanosheet/CNT coupling layer for exceptional polysulfide recycling performance. Adv. Energy Mater. 8, 1800710.
- 16. Yao, S., Cui, J., Deng, Y., Chong, W.G., Wu, J., Ihsan-Ul-Haq, M., et al. (2019). Ultrathin Sb<sub>2</sub>S<sub>3</sub> nanosheet anodes for exceptional pseudocapacitive contribution to multi-battery

- charge storage. Energy Storage Mater. 20, 36–45
- Yao, S., Cui, J., Lu, Z., Xu, Z.L., Qin, L., Huang, J., et al. (2017). Unveiling the unique phase transformation behavior and sodiation kinetics of 1D van der Waals Sb<sub>2</sub>S<sub>3</sub> anodes for sodium ion batteries. Adv. Energy Mater. 7, 1602149.
- Xie, F., Zhang, L., Gu, Q., Chao, D., Jaroniec, M., and Qiao, S.Z. (2019). Multi-shell hollow structured Sb<sub>2</sub>S<sub>3</sub> for sodium-ion batteries with enhanced energy density. Nano Energy 60, 591–599.
- 19. Lakshmi, V., Chen, Y., Mikhaylov, A.A., Medvedev, A.G., Sultana, I., Rahman, M.M., et al. (2017). Nanocrystalline  $\mathrm{SnS}_2$  coated onto reduced graphene oxide: demonstrating the feasibility of a non-graphitic anode with sulfide chemistry for potassium-ion batteries. Chem. Commun. (Camb.) 53, 8272–8275.
- Cui, J., Yao, S., Lu, Z., Huang, J.Q., Chong, W.G., Ciucci, F., et al. (2018). Revealing pseudocapacitive mechanisms of metal dichalcogenide SnS<sub>2</sub>/graphene-CNT aerogels for high-energy Na hybrid capacitors. Adv. Energy Mater. 8, 1702488.
- Zhang, F., Xia, C., Zhu, J., Ahmed, B., Liang, H., Velusamy, D.B., et al. (2016). SnSe<sub>2</sub> 2D anodes for advanced sodium ion batteries. Adv. Energy Mater. 6, 1601188.
- Tan, H., Feng, Y., Rui, X., Yu, Y., and Huang, S. (2020). Metal chalcogenides: paving the way for high-performance sodium/potassium-ion batteries. Small Methods 4, 1900563.
- Hu, M., Ju, Z., Bai, Z., Yu, K., Fang, Z., Lv, R., and Yu, G. (2020). Revealing the critical factor in metal sulfide anode performance in sodiumion batteries: an investigation of polysulfide shuttling issues. Small Methods 4, 1900673.
- 24. Zhang, Q., Tan, S., Mendes, R.G., Sun, Z., Chen, Y., Kong, X., et al. (2016). Extremely weak van der Waals coupling in vertical ReS<sub>2</sub> nanowalls for high-current-density lithium-ion batteries. Adv. Mater. 28, 2616–2623.
- Liu, Y., Yu, X.Y., Fang, Y., Zhu, X., Bao, J., Zhou, X., et al. (2018). Confining SnS<sub>2</sub> ultrathin nanosheets in hollow carbon nanostructures for efficient capacitive sodium storage. Joule 2, 725, 735
- Sun, D., Ye, D., Liu, P., Tang, Y., Guo, J., Wang, L., et al. (2018). MoS<sub>2</sub>/Graphene nanosheets from commercial bulky MoS<sub>2</sub> and graphite as anode materials for high rate sodium-ion batteries. Adv. Energy Mater. 8, 1702383.
- Wang, C., Ma, Z., Wang, Y., and Lu, C. (2016). Failure prediction of high-capacity electrode materials in lithium-ion batteries.
   J. Electrochem. Soc. 163, A1157–A1163.
- Fan, Z., Zhang, L., Baumann, D., Mei, L., Yao, Y., Duan, X., Shi, Y., Huang, J., Huang, Y., and Duan, X. (2019). In situ transmission electron microscopy for energy materials and devices. Adv. Mater. 31, 1900608.
- Shang, T., Wen, Y., Xiao, D., Gu, L., Hu, Y.S., and Li, H. (2017). Atomic-scale monitoring of electrode materials in lithium-ion batteries using in situ transmission electron microscopy. Adv. Energy Mater. 7, 1700709.

- Qian, D., Ma, C., More, K.L., Meng, Y.S., and Chi, M. (2015). Advanced analytical electron microscopy for lithium-ion batteries. NPG Asia Mater. 7. e193.
- Yuan, Y., Amine, K., Lu, J., and Shahbazian-Yassar, R. (2017). Understanding materials challenges for rechargeable ion batteries with in situ transmission electron microscopy. Nat. Commun. 8, 1–14.
- Tan, J., Liu, D., Xu, X., and Mai, L. (2017). In situ/ operando characterization techniques for rechargeable lithium-sulfur batteries: a review. Nanoscale 9, 19001–19016.
- Liu, D., Shadike, Z., Lin, R., Qian, K., Li, H., Li, K., Wang, S., Yu, Q., Liu, M., Ganapathy, S., et al. (2019). Review of recent development of in situ/ operando characterization techniques for lithium battery research. Adv. Mater. 31, 1806620
- Chen, M., Chou, S., and Dou, S. (2019). Understanding challenges of cathode materials for sodium-ion batteries using synchrotron-based X-ray absorption spectroscopy. Batter. Supercaps 2, 842–851.
- 35. Lin, F., Liu, Y., Yu, X., Cheng, L., Singer, A., Shpyrko, O.G., Xin, H.L., Tamura, N., Tian, C., Weng, T.C., et al. (2017). Synchrotron X-ray analytical techniques for studying materials electrochemistry in rechargeable batteries. Chem. Rev. 117, 13123–13186.
- Zhang, Y., Hu, L.P., Zhu, T.J., Xie, J., and Zhao, X.B. (2013). High yield Bi<sub>2</sub>Te<sub>3</sub> single crystal nanosheets with uniform morphology via a solvothermal synthesis. Cryst. Growth Des. 13, 645–651.
- Akbari Garakani, M., Abouali, S., Cui, J., and Kim, J.K. (2018). In situ TEM study of lithiation into a PPy coated α-MnO<sub>2</sub>/graphene foam freestanding electrode. Mater. Chem. Front. 2, 1481–1488.
- Cui, J., Xu, Z.L., Yao, S., Huang, J., Huang, J.Q., Abouali, S., et al. (2016). Enhanced conversion reaction kinetics in low crystallinity SnO<sub>2</sub>/CNT anodes for Na-ion batteries. J. Mater. Chem. A 4, 10964–10973.
- Cui, J., Yao, S., Huang, J.Q., Qin, L., Chong, W.G., Sadighi, Z., et al. (2017). Sb-doped SnO<sub>2</sub>/ graphene-CNT aerogels for high performance Li-ion and Na-ion battery anodes. Energy Storage Mater. 9, 85–95.
- Tang, K., Yu, X., Sun, J., Li, H., and Huang, X. (2011). Kinetic analysis on LiFePO₄ thin films by CV, GITT, and EIS. Electrochim. Acta 56, 4869– 4875
- 41. Ihsan-Ul-Haq, M., Huang, H., Wu, J., Cui, J., Yao, S., Chong, W.G., et al. (2020). Thin solid electrolyte interface on chemically bonded Sb<sub>2</sub>Te<sub>3</sub>/CNT composite anodes for high performance sodium ion full cells. Nano Energy 71, 104613.
- Cui, J., Zheng, H., and He, K. (2020). In situ TEM study on conversion-type electrodes for rechargeable ion batteries. Adv. Mater. 2000 699 https://doi.org/10.1002/adma. 202000699.
- 43. Kim, S., Cui, J., Dravid, V.P., and He, K. (2019). Orientation-dependent intercalation channels

## **Matter** Article



- for lithium and sodium in black phosphorus. Adv. Mater. 31, 1904623.
- 44. Kim, S., Yao, Z., Lim, J.M., Hersam, M.C., Wolverton, C., Dravid, V.P., and He, K. (2018). Atomic-scale observation of electrochemically reversible phase transformations in SnSe<sub>2</sub> single crystals. Adv. Mater. 30, 1804925.
- 45. McDowell, M.T., Lee, S.W., Harris, J.T., Korgel, B.A., Wang, C., Nix, W.D., and Cui, Y. (2013). In situ TEM of two-phase lithiation of amorphous silicon nanospheres. Nano Lett. 13, 758-764.
- 46. Sun, J., Lee, H.W., Pasta, M., Yuan, H., Zheng, G., Sun, Y., Li, Y., and Cui, Y. (2015). A phosphorene-graphene hybrid material as a high-capacity anode for sodium-ion batteries. Nat. Nanotechnol. 10, 980-985.
- 47. He, K., Zhang, S., Li, J., Yu, X., Meng, Q., Zhu, Y., Hu, E., Sun, K., Yun, H., Yang, X.Q., et al. (2016). Visualizing non-equilibrium lithiation of spinel oxide via in situ transmission electron microscopy. Nat. Commun. 7, 1–9.
- 48. Li, J., He, K., Meng, Q., Li, X., Zhu, Y., Hwang, S., Sun, K., Gan, H., Zhu, Y., Mo, Y., et al. (2016). Kinetic phase evolution of spinel cobalt oxide during lithiation. ACS Nano 10, 9577-9585.
- 49. Liu, W.R., Guo, Z.Z., Young, W.S., Shieh, D.T., Wu, H.C., Yang, M.H., and Wu, N.L. (2005). Effect of electrode structure on performance of

- Si anode in Li-ion batteries: Si particle size and conductive additive. J. Power Sources 140,
- 50. Mukaibo, H., Yoshizawa, A., Momma, T., and Osaka, T. (2003). Particle size and performance of SnS<sub>2</sub> anodes for rechargeable lithium batteries. J. Power Sources 119-121, 60-63.
- 51. Hart, G.L.W., and Forcade, R.W. (2008). Algorithm for generating derivative structures. Phys. Rev. B Condens. Matter Mater. Phys. 77,
- 52. Urban, A., Seo, D.H., and Ceder, G. (2016). Computational understanding of Li-ion batteries. NPJ Comput. Mater. 2, 1-13.
- 53. Zhang, Z., Ramos, E., Lalère, F., Assoud, A., Kaup, K., Hartman, P., et al. (2018). Na<sub>11</sub>Sn<sub>2</sub>PS<sub>12</sub>: a new solid state sodium superionic conductor. Energy Environ. Sci. 11,
- 54. Zhu, Y., and Wang, C. (2010). Galvanostatic intermittent titration technique for phasetransformation electrodes. J. Phys. Chem. C 114, 2830-2841.
- 55. Huang, S., Fan, F., Li, J., Zhang, S., and Zhu, T. (2013). Stress generation during lithiation of high-capacity electrode particles in lithium ion batteries. Acta Mater. 61, 4354-4364.

- 56. Perdew, J.P., Burke, K., and Ernzerhof, M. (1996). Generalized gradient approximation made simple. Phys. Rev. Lett. 77, 3865–3868.
- 57. Joubert, D. (1999). From ultrasoft pseudopotentials to the projector augmentedwave method. Phys. Rev. B Condens. Matter Mater. Phys. 59, 1758–1775.
- 58. Giannozzi, P., Baroni, S., Bonini, N., Calandra, M., Car, R., Cavazzoni, C., Ceresoli, D., Chiarotti, G.L., Cococcioni, M., Dabo, I., et al. (2009). Quantum ESPRESSO: a modular and open-source software project for quantum simulations of materials. J. Phys. Condens. Matter 21, 395502.
- 59. Pack, J.D., and Monkhorst, H.J. (1977). "Special points for Brillouin-zone integrations"-a reply. Phys. Rev. B 16, 1748-1749.
- 60. Henkelman, G., Uberuaga, B.P., and Jónsson, H. (2000). Climbing image nudged elastic band method for finding saddle points and minimum energy paths. J. Chem. Phys. 113, 9901-9904.
- 61. Golesorkhtabar, R., Pavone, P., Spitaler, J., Puschnig, P., and Draxl, C. (2013). ElaStic: a tool for calculating second-order elastic constants from first principles. Comput. Phys. Commun. 184, 1861-1873.